

See discussions, stats, and author profiles for this publication at: <https://www.researchgate.net/publication/3202107>

# Unmixing-based multisensor multiresolution image fusion

Article in IEEE Transactions on Geoscience and Remote Sensing · June 1999

DOI: 10.1109/36.763276 · Source: IEEE Xplore

CITATIONS

277

READS

826

4 authors, including:



**Boris Sergeevich Zhukov**

Space Research Institute

136 PUBLICATIONS 1,830 CITATIONS

[SEE PROFILE](#)



**Dieter Oertel**

Astro-und Feinwerktechnik Adlershof GmbH

182 PUBLICATIONS 1,782 CITATIONS

[SEE PROFILE](#)

Some of the authors of this publication are also working on these related projects:



BIRD, small satellite [View project](#)



Venus atmosphere research [View project](#)

# Unmixing-Based Multisensor Multiresolution Image Fusion

Boris Zhukov, Dieter Oertel, Franz Lanzl, and Götz Reinhäkel

**Abstract**—Constrained and unconstrained algorithms of the multisensor multiresolution technique (MMT) are discussed. They can be applied to unmix low-resolution images using the information about their pixel composition from co-registered high-resolution images. This makes it possible to fuse the low- and high-resolution images for a synergetic interpretation. The constrained unmixing preserves all the available radiometric information of the low-resolution image. On the other hand, the unconstrained unmixing may be preferable in case of noisy data. An analysis of the MMT sensitivity to sensor errors showed that the strongest requirement is the accuracy of geometric co-registration of the data; the co-registration errors should not exceed 0.1–0.2 of the low-resolution pixel size. Applications of the constrained and unconstrained algorithms are illustrated on examples of unmixing and fusion of the multiresolution reflective and thermal bands of a real TM/LANDSAT image as well as of a simulated image of the future ASTER/EOS-AM1 sensor.

**Index Terms**—Image processing, image reconstruction, inverse problems, multisensor systems, remote sensing.

## NOMENCLATURE

ASTER	Advanced Spaceborne Thermal Emission and Radiation Radiometer of the EOS-AM1 mission.
CI	Classifying instrument.
MI	Measuring instrument.
MIR	Middle infrared spectral range (3–5 $\mu\text{m}$ ).
MMT	Multisensor multiresolution technique.
PSF	Point spread function.
SWIR	Short-wave infrared spectral range (1.1–2.5 $\mu\text{m}$ ).
TIR	Thermal infrared spectral range (8–12 $\mu\text{m}$ ).
TM	Thematic Mapper scanner on LANDSAT satellites.
VNIR	Visible and near-infrared spectral range (0.4–1.1 $\mu\text{m}$ ).

## I. PROBLEM

**F**USION of multisensor imaging data enables a synergetic interpretation of complementary information obtained by sensors of different spectral ranges (from the visible to the microwave) and/or with different number, position, and width of spectral bands [1], [2].

Manuscript received July 1, 1998; revised October 28, 1998.

B. Zhukov is with the Space Research Institute of the Russian Academy of Sciences, Moscow, Russia, on leave at the DLR Institute of Optoelectronics, 82234 Oberpfaffenhofen, Germany (e-mail: zhukov@zeus.oe.op.dlr.de).

D. Oertel, F. Lanzl, and G. Reinhäkel are with the DLR Institute of Optoelectronics, 82234 Oberpfaffenhofen, Germany.

Publisher Item Identifier S 0196-2892(99)03457-9.

A specific feature of multisensor data sets is often the difference in spatial resolution of the various sensors (channels). This is caused, on the one hand, by requirements of many applications for a high spatial resolution and, on the other hand, by physical and technological limitations that make it unfeasible to obtain an equally high resolution at different wavelengths and in channels with different bandwidths.

In particular, detailed land-oriented applications require usually a resolution of several meters to several tens of meters since otherwise a large number of image pixels may represent a mixture of different objects. These “mixed” pixels is one of the principal sources of errors in satellite image interpretation. However, the required high spatial resolution is provided only by panchromatic and multispectral scanners in the reflective spectral range (e.g., HRV/SPOT, MOMS-02 on the Shuttle D-2 mission and on PRIRODA module of the MIR station, the reflective channels of TM/LANDSAT and ASTER/EOS-AM1) as well as by SAR sensors (e.g., on ERS-1,2, ALMAZ, and RADARSAT). Other types of satellite imaging sensors like imaging spectrometers (MERIS/ENVISAT-1), thermal scanners (the thermal channels of TM/LANDSAT and ASTER/EOS-AM1), and imaging microwave radiometers (SSM/I on DMSP) could provide additional useful information, e.g., about biochemical composition of vegetation and waters, mineralogical composition of soils and rocks, surface temperature, water content in vegetation and soil, etc. However, their resolution from about 100 m for thermal scanners up to tens of kilometers for microwave radiometers leads to a large number of mixed pixels in their data preventing their efficient utilization for many land-oriented applications.

One of the possible approaches in a multisensor data environment is to use the data of higher resolution sensors/channels to analyze the composition of mixed pixels in images obtained by lower resolution sensors/channels in order to unmix them.

The purpose of this paper is to present the multisensor multiresolution technique (MMT) that may be a useful tool for these tasks. We discuss the context of the MMT development in Section II, its algorithm in Section III, and its application conditions and limitations in Section IV. After that, MMT applications are illustrated in Section V on examples of unmixing/fusion of multiresolution reflective and thermal bands of a TM/LANDSAT-5 image as well as of a simulated ASTER/EOS-AM1 image. Conclusions and recommendations for MMT application are given in Section VI.

## II. BACKGROUND

The term “image fusion (merge)” is used throughout this paper as a synonym of the “pixel-level fusion” according to

the terminology [3] and corresponds to merging of measured radiances, e.g., for a combined retrieval of surface/atmosphere parameters. The “feature-level fusion” and “decision-level fusion,” which correspond more to statistical recognition tasks, are beyond the scope of this paper.

The multiresolution image fusion (merging) techniques [3], [4] merge the spatial information from a “high-resolution” image with the radiometric information from a “low-resolution” image. The process can also be considered as sharpening of the low-resolution image. The terms “high-resolution” and “low-resolution” are used here in a relative sense for the given combination of two images. Many of the image sharpening techniques have been developed for the specific case when the high-resolution image has only one spectral band as in the case of merging panchromatic and multispectral images as obtained, e.g., by HRV/SPOT. We will deal with the general case when the high-resolution image may be multispectral.

The available constraints for a radiometrically accurate reconstruction of a sharpened image in the low-resolution bands but with the high-resolution pixel size are the “energy balance” requirements: 1) if the sharpened image is degraded again to the original low resolution, it should coincide with the original low-resolution image, and 2) if spectral bands of the high-resolution image can be fitted by the spectral bands of the low-resolution image, then it is additionally required that the corresponding spectral degradation of the sharpened image should reproduce the high-resolution band images. These constraints are obviously insufficient to obtain an unambiguous solution for the sharpened image. It has been proposed to choose the minimum-norm pseudoinverse [5], [6] or the first local minimum along the projected gradient [7] as the unique solution from the infinite set of possible solutions for the sharpened low-resolution image. However, there is hardly any practical reason to prefer *a priori* these solutions to other possible solutions.

Comparative studies [8], [9] show that the techniques, which perform the most radiometrically accurate sharpening, are usually not those that produce synthetic images with the best visual impression. The latter is obtained by enhancing the effect of the high-resolution image texture in the sharpened image even at the expense of distorting its radiometric accuracy. In this paper, we will analyze the image fusion techniques using their radiometric accuracy as the principal criterion.

The image sharpening techniques are usually divided into spectral component substitution techniques and spatial domain techniques.

*The spectral component substitution techniques* have been developed principally for the case of fusion panchromatic and multispectral images. They are based on replacing a spectral component of the low-resolution multispectral image by the radiometrically adjusted panchromatic image. Among the most frequently used spectral component substitution techniques are as follows.

- 1) Intensity-hue-saturation merge [10], [11] substituting the image intensity.
- 2) Principal component merge [8], [12], [13] substituting the first principal component.

- 3) Regression variable substitution (RVS) technique [8] substituting the regression variable obtained by statistical fitting of the high- and low-resolution image.
- 4) the radiometric method [9] substituting the component obtained by spectral fitting of the high- and low-resolution bands (if such fitting is possible).

The RVS technique [8] and the radiometric method [9] provide the best radiometric adjustment of the substituted component. However, a common disadvantage of the spectral component substitution techniques is that all the other spectral components except for the substituted one are left at their original low resolution (their resampling cannot be considered as an actual resolution enhancement).

*The spatial domain techniques* transfer high-resolution information from the high-resolution image to all the low-resolution spectral bands using various deterministic or statistical predictors. In order to preserve the available radiometric information of the low-resolution image, only the excess high spatial frequency components have to be transferred to the low-resolution bands. This can be done by a high pass filtration in the image domain [12], [14], [15] or by using various multiresolution representations: the wavelet decomposition [16]–[19], the Laplacian pyramid [20], [21], or the Fourier decomposition [22].

An appropriate choice of the predictor is critical for radiometric accuracy of the sharpened image. Deterministic predictors [23], [24] are more simple but less accurate than adaptive statistical predictors. Linear statistical predictors [14], [15], [25]–[27] provide good radiometric accuracy if the correlation between the high- and the low-resolution bands is strong. Otherwise, they may lead to strong radiometric distortions in the sharpened image (including contrast inversion). This may be the case, for example, when merging panchromatic and near-infrared images or reflective and thermal images. Better results in such cases can be obtained with nonlinear predictors that assume only predictability of signals in the low-resolution bands from signals in the high-resolution bands rather than a linear relation between them. Examples of nonlinear predictors are the look-up-table predictor [25], the median predictor [28], and the sigma-filter [29].

However, if the relation between the signals in the high- and low-resolution bands is nonlinear, a problem arises with training an adaptive predictor. In this case, the procedure of training the predictor on the available low-resolution image and then to apply it at the high-resolution pixel size may be inaccurate. In particular, the adaptive statistical predictors may not provide a radiometrically accurate fusion if there is a large number of mixed pixels in the low-resolution image.

Mixed pixels in multispectral and hyperspectral images can be analyzed with *spectral “endmember” unmixing techniques* (e.g., [30]–[32]). These techniques use reference spectra of pure spectral classes (“endmembers”) to derive endmember proportions in mixed pixels rather than to reconstruct an actual high-resolution image in the low-resolution bands. An adequate definition of endmembers and of their spectra is necessary to obtain reasonable results. The endmember techniques are not useful with one-band low-resolution images (e.g., with TM/LANDSAT thermal images).

Both unmixing of spatially low-resolution pixels and reconstruction of an image in the low-resolution bands with the high-resolution pixel size can be performed by the MMT [33], [34]. It can be used in cases where most or even all of the low-resolution pixels are mixed. In contrast to the end-member techniques, it does not require spectra of pure classes for the unmixing but retrieves them in the process. The MMT is based on 1) classifying the image of the high-resolution sensor (or sensor channels) and 2) retrieving signals of the low-resolution sensor (or sensor channels) for the classes recognized in the high-resolution data. From this point of view, the high-resolution sensor/channels are conventionally called *the classifying instrument* (CI), while the lower-resolution sensor/channels are called *the measuring instrument* (MI). As an option, high-resolution TM's (where available) can be used instead of the CI data to unmix MI images.

A similar approach to unmix multitemporal multiresolution images obtained by different sensors *in the same spectral bands* has been proposed in [35].

The principal limitation of this class-based unmixing is that the MI-signals are averaged over the total area of each class in the image. A moving window processing can be applied to reduce the spatial scale of the within-class averaging to the selected window size [36]. Alternatively or additionally to the moving window processing, a low pass correction can be used to introduce only excess spatial frequencies in the unmixed MI image while preserving its available low-resolution information [37]. A disadvantage of the low pass correction is that it may produce wave-type artifacts at sharp object borders.

In this paper, a *constrained MMT-unmixing algorithm* for image fusion is proposed to incorporate all the available MI information already in the process of unmixing.

### III. ALGORITHM

The MMT algorithm is adapted to the practical situation in a multisensor data environment when the detailed spatial information is available only in the high-resolution CI image. This information is used to analyze composition of the lower-resolution MI pixels and to unmix them.

The unmixing of the MI pixels is performed consecutively in the moving window mode. In order to unmix the central MI pixel in the window, contextual information of the surrounding MI pixels is essentially used (Fig. 1). In particular, it is assumed that the features, that are recognizable in the high-resolution CI image, have the same MI signals in the central MI pixel as in the surrounding MI pixels in the window.

The algorithm includes the following operations.

- 1) Classification of the CI image.
- 2) Definition of class contributions to the signal of the MI pixels.
- 3) Window-based unmixing of the MI-pixels.
- 4) Reconstruction of an unmixed (sharpened) image.

The first step of the algorithm is a *classification of the high-resolution CI image*. Various unsupervised or supervised algorithms can be used to perform a spectral and/or textural classification of the CI image [38]. The selection of a classification algorithm should depend on a specific application.

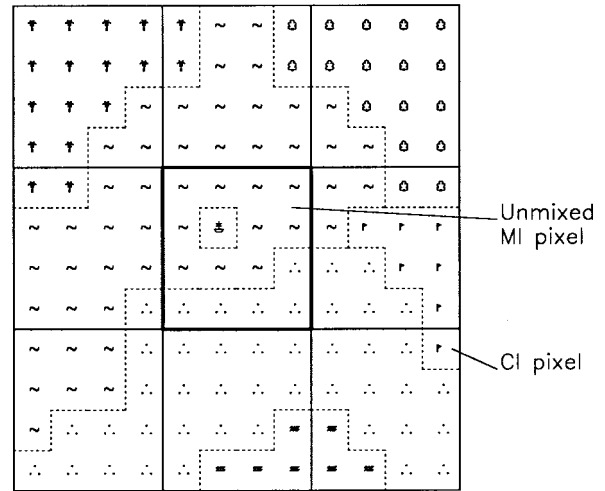


Fig. 1. Geometry of moving-window MMT unmixing: the central MI pixel in the window is unmixed using the information about its composition and about composition of the other MI pixels in the window as provided by the high-resolution CI image.

In this paper we will use for this purpose an unsupervised classification (clustering). This is an appropriate approach for the task of retrieving radiance variations in the scene and interpreting them in terms of physical parameters, e.g., by model inversion.

Though a separate classification of each window is possible [36], a general classification of the entire image may be preferable to avoid the problem of establishing correspondence between the spectral classes identified in different windows.

The result of the classification is a high-resolution classification map  $k(m, n)$  ascribing to the high-resolution pixels  $(m, n)$  a code  $k$  of the corresponding classes. The classes may represent different objects or subobject areas with different physical parameters.

*Definition of class contributions to the signal of the MI pixels* is performed with accounting for both the class area proportion in the MI pixels as given by the classification map  $k(m, n)$  and for the PSF's of the MI channels:

$$c_i(l, s; k_0) = \sum_{k(m, n) \in k_0} \rho_i(l, s; m, n) \quad (1)$$

where  $c_i(l, s; k_0)$  is the contribution of class  $k_0$  to the signal of MI pixel  $(l, s)$  in MI band  $i$ , and  $\rho_i(l, s; m, n)$  is a discrete approximation for the sensor PSF.

The discrete PSF gives the contribution from the area of a high-resolution pixel  $(m, n)$  to the MI signal of pixel  $(l, s)$  in band  $i$ . Its sum over  $(m, n)$  is assumed to be normalized to 1. The PSF should account for the sensor-related effects as well as for the rsampling (if the MI image is resampled to co-register it with the CI image). The atmospheric component should be included in the PSF only if the atmospheric smearing was corrected in the CI image before the classification (or if a ground-based TM is used for unmixing instead of CI data). In this case, the atmospheric smearing will be also removed during the unmixing.

*Unmixing of the MI pixels* is performed consecutively in a window that is moved with the step of 1 MI-pixel size. In each

window, the central MI pixel is unmixed by an inversion of a system of linear mixture equations that are written for all the MI pixels in the window:

$$S_i(l, s) = \sum_{k=1}^K c_i(l, s; k) \bar{S}_i(k) + \varepsilon_i(l, s) \quad (2)$$

where  $S_i(l, s)$  is the signal of MI pixel  $(l, s)$  in the window,  $\bar{S}_i(k)$  is the mean MI-signal for class  $k$  in the window, and  $\varepsilon_i(l, s)$  is the model error. The sources of the model error are sensor errors (radiometric noise, co-registration errors, PSF calibration errors) as well as class heterogeneity that may cause a difference of class signals in various MI pixels from the mean signal  $\bar{S}_i(k)$  in the window.

The inversion of equation system (2) is performed by a least-squares method [39] independently for each MI band. If (2) for the central MI pixel  $(l_0, s_0)$  of the window image is used as a linear constraint during the least-squares inversion (without the error term), it will insure that the “energy balance” requirement for the central pixel will be met (the total signal of the original MI pixel will be preserved). This type of unmixing will be called the constrained unmixing. On the other hand, if all the pixels in the window are taken during the least-squares inversion with the same weight, the unmixing will be called unconstrained. The unconstrained unmixing meets the “energy balance” requirement for the individual classes in the window but not for individual MI pixels.

The inversion problem for (2)—as well as other resolution-enhancement problems—is ill-conditioned, resulting in noise amplification in the solution [40]. In order to stabilize the solution, the least-squares inversion can be performed by minimization of the cost function

$$F = \sum_{(l,s) \neq (l_0,s_0)} \left( S_i(l, s) - \sum_{k=1}^K c_i(l, s; k) \bar{S}_i(k) \right)^2 + \alpha \frac{N_{\text{MI}} - 1}{K} \sum_{k=1}^K (\bar{S}_i(k) - \bar{S}'_i(k))^2 \quad (3)$$

where  $K$  and  $N_{\text{MI}}$  are the number of classes and the number of MI pixels in the window. The first sum in (3) is taken over all the MI pixels in the window, with exclusion of the central pixel  $(l_0, s_0)$  in the case of the constrained unmixing. The second sum in (3) with a regularization parameter  $\alpha$  is added for regularization of the solution. It limits large deviations of the MI class signals  $\bar{S}_i(k)$  from preset class signals  $\bar{S}'_i(k)$ . The factor  $(N_{\text{MI}} - 1)/K$  is introduced to make  $\alpha$  independent of the difference in the number of terms in the first and the second sums and thus to characterize better the “weight” of the preset class signals during the unmixing (in the case of the unconstrained unmixing this factor should be  $N_{\text{MI}}/K$ ).

The regularization makes it possible to decrease the retrieval errors that may be large for small classes (see discussion in Section IV). A possible choice of the preset MI class signals  $\bar{S}'_i(k)$  is the median value of the MI-image over the class area in the window as provided by the median-sharpening technique [28].

The choice of the regularization parameter  $\alpha$  is a general problem of regularization techniques: a too-large  $\alpha$  would lead

to smearing of the unmixed image, while a too-small  $\alpha$  would not allow to suppress the large retrieval errors for small classes. A few algorithms for an “optimal” regularization parameter selection have been proposed, e.g., the discrepancy principle, the generalized cross-validation, and the L-curve [40], [41]. A simple visual check of the unmixed image can also be helpful: the value of  $\alpha$  should be decreased until a “pepper-like” noise (corresponding to large retrieval errors for small classes) starts to appear in the unmixed image.

*Restoration of the unmixed MI-image*  $H_i^*(m, n)$  is performed by assigning the estimated mean class signals  $\bar{S}_i^*(k)$  to the corresponding high-resolution pixels of the classification map:

$$H_i^*(m, n) = \bar{S}_i^*(k(m, n)), \quad (m, n) \in (l_0, s_0). \quad (4)$$

This assignment is performed in each window only within the area of its central MI pixel  $(l_0, s_0)$  (that meets the “energy balance” requirement if the constrained unmixing is applied). As the window moves over the image with the step of 1 MI pixel size, the entire unmixed image is reconstructed pixel by pixel.

#### IV. MMT APPLICATION ASPECTS AND LIMITATIONS

##### A. Number of Classes and Their Separability

The general condition of existence of the least-squares solution for equation system (2) is

$$\det(A_i(k, k')) \neq 0 \quad (5)$$

where

$$A_i(k, k') = \sum_{l,s} c_i(l, s; k) c_i(l, s; k'). \quad (6)$$

Condition (5) depends on the MI band  $i$  since various MI channels may have different point spread functions.

In particular, (5) limits the allowed number of classes  $K$  in the window: it should not exceed the number of the MI pixels in the window  $N_{\text{MI}}$  for the unconstrained unmixing and should be less than  $N_{\text{MI}}$  for the constrained unmixing. Moreover, it may be recommended to reduce further this maximal allowed number of classes a factor of  $\sim 2$  for stability of the inversion. However, this does not yet guarantee existence of the solution. A typical situation of this type occurs when two or more small objects are present in only one MI pixel and do not appear anywhere else. It is clear that in this case it is impossible to separate their MI signals.

In our algorithm, when (3) cannot be resolved for some window in at least one MI band, then the smallest class in the window is combined with the spectrally closest class until (5) is met.

##### B. Unmixing Capability

The MMT unmixing can be performed only relative those classes that can be recognized in the high-resolution CI image. If a class is homogeneous only in the CI spectral bands but heterogeneous in the MI bands, averaging of its MI signature

will take place over the class area in the window (with accounting for all available low-resolution MI information by the constrained algorithm). If class areas with different MI signatures are located in different windows, they will be treated independently, and no averaging of their MI signatures will take place. Thus, the MMT unmixing can be efficient for a specific application if the classes, which are essential for this application, can be differentiated spectrally in CI data and/or can be separated spatially.

Let us consider the signal restoration error for a high-resolution pixel  $(m, n)$  in the unmixed MI image:

$$\begin{aligned}\Delta_i^{\text{unmix}}(m, n) &= H_i^*(m, n) - H_i(m, n) \\ &= (\bar{S}_i^*(k) - \bar{S}_i(k)) + (\bar{S}_i(k) - H_i(m, n)) \\ &= \Delta_i^{\text{class}}(k) + \Delta_i^{\text{in-class}}(m, n).\end{aligned}\quad (7)$$

Here  $H_i(m, n)$  is the hypothetical ideal image that would be obtained in the MI spectral bands with the high-resolution pixel size. The pixel restoration error (7) has two components: 1) the retrieval error  $\Delta_i^{\text{class}}(k)$  of the mean MI-signal for class  $k$ , to which pixel  $(m, n)$  is ascribed during the classification, and 2) the deviation  $\Delta_i^{\text{in-class}}(m, n)$  of this mean class signal from the true MI-signal of pixel  $(m, n)$  due class heterogeneity in the window.

The standard deviation  $\sigma_i^{\text{class}}(k)$  of the class signal retrieval errors  $\Delta_i^{\text{class}}(k)$  can be estimated from the residuals of the linear mixture model (2) [39]. It tends to increase as the area of the class in the window decreases. Let us consider as an example a simple scene that is composed of a small subpixel object (class 1) observed at a homogeneous background (class 2). Let  $c(1)$  and  $(1 - c(1))$  be the contributions of the object and of the background correspondingly to the MI signal of the pixel where the object is located. The other pixels are assumed to contain only the background. Then, it can be obtained from (2) that the standard deviation of the retrieved signal for the object is equal to

$$\sigma^{\text{class}}(1) = \frac{\sqrt{\sigma_0^2 + (1 - c(1))^2 \sigma^{\text{class}^2}(2)}}{c(1)} \approx \frac{\sigma_0}{c(1)} \quad (8)$$

where  $\sigma_0$  is the standard deviation of the error of model (2). It has been taken into account in (8) that the standard deviation of the retrieval error for the background signal is  $\sigma^{\text{class}}(2) \approx \sigma_0 / \sqrt{N_{\text{MI}} - 1}$  and can be neglected in comparison to  $\sigma_0$ . Thus, though there are no principal limitations of the minimal area of classes [provided that (5) is met], large retrieval errors for small classes can be expected, with their standard deviation being inversely proportional to the class area.

On the contrary, the class-heterogeneity error component  $\Delta_i^{\text{in-class}}(m, n)$  should decrease with an increasing detail of classification to the limit defined by the CI differentiating capability. This error cannot be estimated only from the available data. A way to reduce the effect of the class-heterogeneity error is to interpret the merged CI/MI image not at the level of high-resolution pixels but rather at the level of extended features that can be recognized in it. The borders of these features will be defined principally by the class borders in the high-resolution classification map, with a

possible modification due to the low-resolution MI information that is preserved in the unmixed MI image. Averaging over the pixels belonging to the same class will reduce the deviation of their mean MI signal from the mean class MI-signal.

### C. Window Size

The selection of the window size is governed by two factors: 1) the window size should be as small as possible to reduce the spatial averaging scale of the MI class signatures and 2) the window should contain a sufficient number of MI pixels for a stable inversion. Our experiments have shown that the minimal window of  $3 \times 3$  MI pixels can be used only with rather rough classification maps since it limits significantly the allowed number of classes. Additionally, the  $3 \times 3$  window proved to be more sensitive than larger windows to sensor errors and to variations in the regularization parameter.

A larger window of  $5 \times 5$  MI pixels was found to be a good compromise between an acceptable scale of spatial averaging, the allowed number of classes, and the stability of the inversion. If a regularization is not used, a still larger window may be required to stabilize the solution [42].

## V. EXAMPLES OF MMT-UNMIXING

We will illustrate MMT application on examples of unmixing and fusion of multiresolution visible and near infrared (VNIR), short-wave infrared (SWIR), and thermal infrared (TIR) bands. For this purpose, a simulated- and a real TM/LANDSAT image as well as a simulated ASTER/EOS-AM1 image are used. Simulation allows to check the unmixing accuracy as well as to analyze sensitivity of the technique to sensor errors. High spatial resolution hyperspectral images obtained by the Digital Airborne Imaging Spectrometer DAIS-7915 [43] on board a Do-228 aircraft were used for the simulation. The spectral bands and the pixel size (sampling step) of the TM/LANDSAT, ASTER/EOS-AM1, and DAIS-7915 are compared in Table I.

Further MMT applications for panchromatic/multispectral and multispectral/hyperspectral image fusion can be found in [36] and [37].

### A. TM/LANDSAT Image

TM/LANDSAT scanner has six VNIR and SWIR bands with the pixel size of 30 m and one TIR band with the pixel size of 120 m (Table I). Unmixing of its thermal band and its fusion with the reflective bands can be useful, e.g., for agricultural and microclimatologic applications [28].

The MMT unmixing was applied to a TM/LANDSAT-5 subscene of an agricultural area at the Querfurter Platte (Germany), which was imaged on May 30, 1996. The subscene contains  $512 \times 384$  pixels with the size of 30 m.

Two image stripes of the same area were obtained by DAIS-7915 within 50 min after the LANDSAT-5 overflight. The two DAIS-7915 image stripes contain  $512 \times 1910$  and  $512 \times 1949$  hyperspectral pixels with the size of  $\sim 6$  m.

The following processing steps were performed to simulate the TM image from the higher-resolution DAIS-7915 image in the region where they overlap (see [42] for details).

TABLE I  
SPECTRAL BANDS AND PIXEL SIZE OF TM/LANDSAT,  
ASTER/EOS-AM1, AND DAIS-7915

Sensor	Spectral range	Spectral bands, $\mu\text{m}$	Pixel size, m
TM (LANDSAT)	VNIR	0.45-0.52, 0.52-0.60, 0.63-0.69, 0.76-0.90	30
	SWIR	1.55-1.75, 2.08-2.35	30
	TIR	10.4-12.5	120
ASTER (EOS-AM1)	VNIR	0.52-0.60, 0.63-0.69, 0.76-0.86	15
	SWIR	1.6-1.7, 2.145-2.185, 2.185-2.225, 2.235-2.285, 2.295-2.365, 2.360-2.430	30
	TIR	8.125-8.475, 8.475-8.825, 8.925-9.275, 10.25-10.95, 10.95-11.65	90
DAIS-7915	VNIR	32 bands in the range of 0.47-1.09 $\mu\text{m}$ with the bandwidth of 0.02-0.03 $\mu\text{m}$	6
	SWIR	40 bands in the range of 1.48-2.50 $\mu\text{m}$ with the bandwidth of 0.03-0.06 $\mu\text{m}$	6
	MIR	3-5	6
	TIR	8.2-9.1, 9.1-9.8, 9.8-10.6, 10.4-11.4, 11.0-12.2, 11.9-13.5	6

- 1) Geometric coregistration of the TM and DAIS-7915 images with the accuracy of within 1 TM reflective pixel (0.25 of the TM thermal pixel size).
- 2) Spectral aggregation of the DAIS-7915 bands to simulate the TM spectral bands by fitting of their spectral response functions.
- 3) Degradation of the spatial resolution of the DAIS-7915 images by their convolution with a Gaussian PSF.
- 4) Radiometric intercalibration of the DAIS-7915 and TM thermal images and their absolute calibration in at-ground temperatures using results of on-ground measurements.

The  $2\sigma$ -width of the Gaussian PSF in the reflective channels was chosen to be equal to the sampling step of 30 m. The PSF width in the TM thermal channel was defined by fitting the simulated and real TM thermal images and turned out to be equal to 160 m. This value was used further during unmixing of the real TM image.

The residual standard deviation of the real and simulated thermal TM images was 2.1 K. It may be explained by

- 1) errors of the TM/DAIS-7915 geometric co-registration;
- 2) relatively strong striping noise in the TM image of up to 0.8 K;
- 3) the difference in the observation time leading to a visible discrepancy in contrast between some fields in the real and simulated images;
- 4) the partial high-altitude semi-transparent cloudiness that is absent in the simulated image but manifests itself in the real TM image by lower signal values in its upper-central part [see Fig. 5(c)].

Additionally, a reference thermal image [see Fig. 5(f)] was generated from the DAIS-7915 data for validation of the MMT unmixing results. The reference image matches the TM thermal image radiometrically, but has the spatial resolution of

30 m. The residual error of the simulated TM thermal image of 2.1 K can be assumed to be the lower limit for the residual error of the reference image (the latter can be expected to be higher, in particular, due to an increased effect of co-registration errors). In order to find the unmixing error  $\sigma_{\text{unmix}}$  of the real TM thermal image, the standard deviation of the unmixed and reference images  $\sigma_{\text{ref}}$  was defined within the area where the both images overlap. In order to separate the effect of the unmixing errors from the effect of the residual error of the reference image, the unmixing error was conventionally defined as  $\sigma_{\text{unmix}} = \sqrt{\sigma_{\text{ref}}^2 - \sigma_{\text{residual}}^2}$ , with  $\sigma_{\text{residual}} = 2.1$  K. It can be expected to be the upper limit for the unmixing error due to a possible under-estimation of the residual error of the reference image. The unmixing error of the simulated TM thermal image was defined directly as its standard deviation from the reference image.

The iterative ISODATA clustering algorithm [38] with a fixed number of spectral classes (clusters) was used for classification of the real and simulated TM images in the six higher resolution reflective bands. The clustering was performed with  $K_0 = 4-64$  classes to investigate the influence of the number of classes on the unmixing accuracy. If after an iteration some of the classes proved to be empty, the initial number of the not-empty classes was restored by dividing the most populated classes into two. The iterations were stopped as soon as less than 0.1% of the pixels changed their class. Finally, an adaptive median filtering with the window of  $3 \times 3$  pixels was applied to the classification maps to filter out isolated points.

The unmixing of the real and simulated TM images was performed with the window size of  $5 \times 5$  thermal pixels, by using, for the regularization, the images sharpened by the median-predictor algorithm [28].

Fig. 2 illustrates the influence of the regularization parameter  $\alpha$  on the accuracy of the constrained and unconstrained unmixing. In the ideal case of the simulated image with no sensor-related errors, the minimal unmixing error of  $\sim 1.6$  K was provided by the constrained algorithm at  $\alpha = 0.3-0.5$ . Generally, the constrained unmixing requires more regularization than the unconstrained unmixing since using the constraint destabilizes additionally the solution.

The errors of the unconstrained unmixing of the simulated image were significantly higher, except for  $\alpha < 0.01$ . At  $\alpha > 1$ , where the median-sharpened regularization image dominates, the error of the unconstrained unmixing for the ideal simulated image was even higher than for the larger real TM scene.

On the contrary, the unconstrained algorithm provided a better accuracy than the constrained one for the real noisy TM image, with  $\sigma_{\text{unmix}} \approx 2.0$  K at  $\alpha = 0.5$ . In the case of the constrained unmixing, the retrieval errors dominated at this noise level over the effect of spatial sharpening. As a result,  $\sigma_{\text{unmix}}$  increased monotonously with decreasing  $\alpha$ .

It is important to note that a variation of the regularization parameter  $\alpha$  in a rather large range of 0.1–1 does not lead to a significant deterioration of the unmixing accuracy in comparison to the optimal selection of  $\alpha$  if a proper algorithm (constrained or unconstrained) is selected in each case.

The effect of the number of classes on the unmixing error is illustrated in Fig. 3. During the constrained and unconstrained

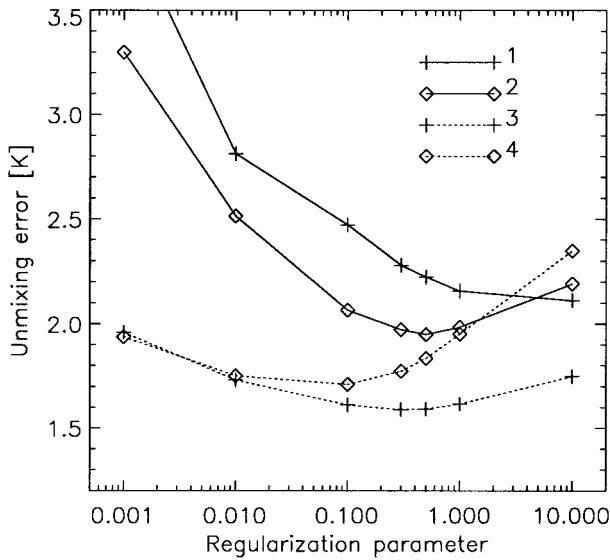


Fig. 2. Unmixing error of the TM thermal image  $\sigma_{\text{unmix}}$  as a function of the regularization parameter  $\alpha$  ( $K_0 = 16$ ): 1—constrained unmixing of the real TM image; 2—unconstrained unmixing of the real TM image; 3—constrained unmixing of the simulated TM image; 4—unconstrained unmixing of the simulated TM image.

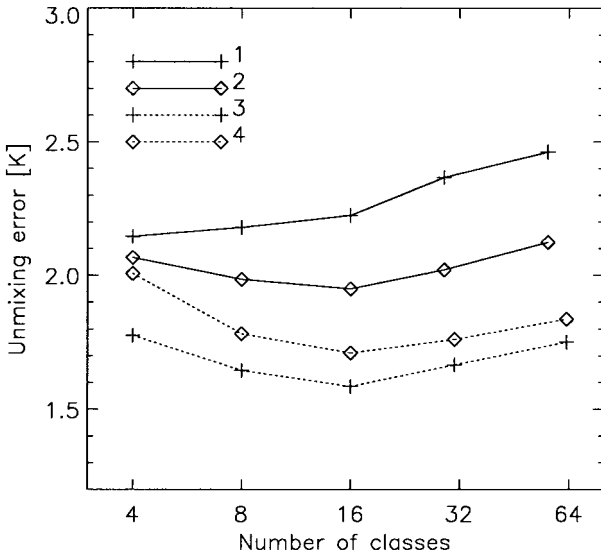


Fig. 3. Unmixing error of the TM thermal image  $\sigma_{\text{unmix}}$  as a function of the number of classes  $K_0$  in the classification map ( $\alpha = 0.5$ ): 1—constrained unmixing of the real TM image; 2—unconstrained unmixing of the real TM image; 3—constrained unmixing of the simulated TM image; 4—unconstrained unmixing of the simulated TM image.

unmixing of the simulated image, as well as during the unconstrained unmixing of the real TM image, the minimal error  $\sigma_{\text{unmix}}$  was achieved with  $K_0 = 10$ – $20$  classes in the classification map. It corresponded to the mean value of  $K = 8$ – $12$  classes in the  $5 \times 5$  moving window and of 5–8 classes in the central thermal pixel. At a larger number of classes, the growing class signal retrieval errors  $\Delta_i^{\text{class}}$  begin to dominate in the total unmixing error (7). At a smaller number of classes, the unmixing error increases due to an

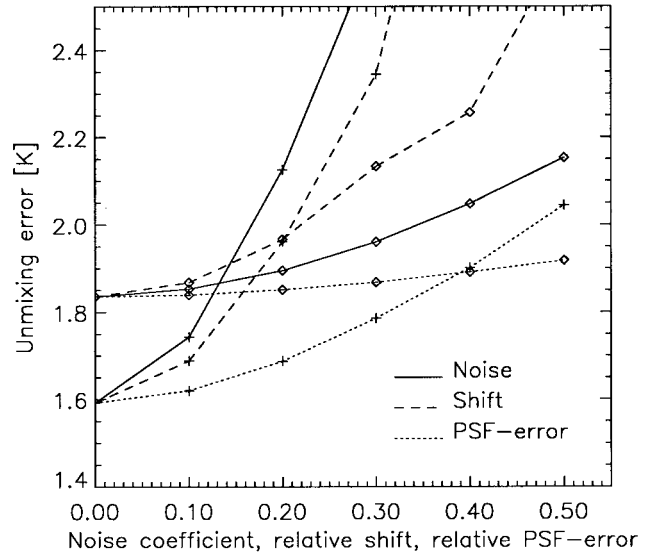


Fig. 4. Effect of noise, of relative shift, and of relative PSF-error on the unmixing error  $\sigma_{\text{unmix}}$  of the simulated TM thermal image ( $\alpha = 0.5$ ,  $K_0 = 16$ ): crosses—constrained unmixing; diamonds—unconstrained unmixing.

insufficient detail of classification, leading to an increase of the class heterogeneity as characterized by the  $\Delta^{\text{in-class}}$  term in (7).

When the constrained unmixing of the real TM image with a high noise level was performed, the effect of the class signal retrieval errors  $\Delta_i^{\text{class}}$  always dominated, leading to a monotonous increase of  $\sigma_{\text{unmix}}$  with the increasing number of classes.

In order to study in more detail the effect of sensor-related errors on the accuracy of the MMT unmixing, the following errors were introduced in the simulated TM image:

- 1) an uncorrelated Gaussian noise with the noise coefficient defined as the ratio of the standard deviations of the noise- and scene signals;
- 2) relative shifts of band images both in the direction of the lines and columns to simulate interchannel coregistration errors.

Additionally, the unmixing was performed with a wider PSF than the one used for the simulation.

Fig. 4 illustrates the separate effects of the errors in the thermal image on the unmixing accuracy. The effect of the similar errors in the high-resolution reflective images was found to be much smaller. The unmixing error of the constrained algorithm at a low level of sensor errors is significantly smaller than of the unconstrained algorithm. However, it is more sensitive to the sensor errors so that the unconstrained unmixing becomes more preferable at a high level of sensor errors. The noise with a practically reasonable level of within 0.1 of the scene signal variability does not increase significantly the retrieval error. The same is also true for the relative PSF-width error of within 0.1–0.2 of its true value. The greatest effect has the interchannel co-registration accuracy. The coregistration of the CI- and MI-images should be performed with an accuracy of 0.1–0.2 of the MI pixel size in order not to get a significant increase of the unmixing error.



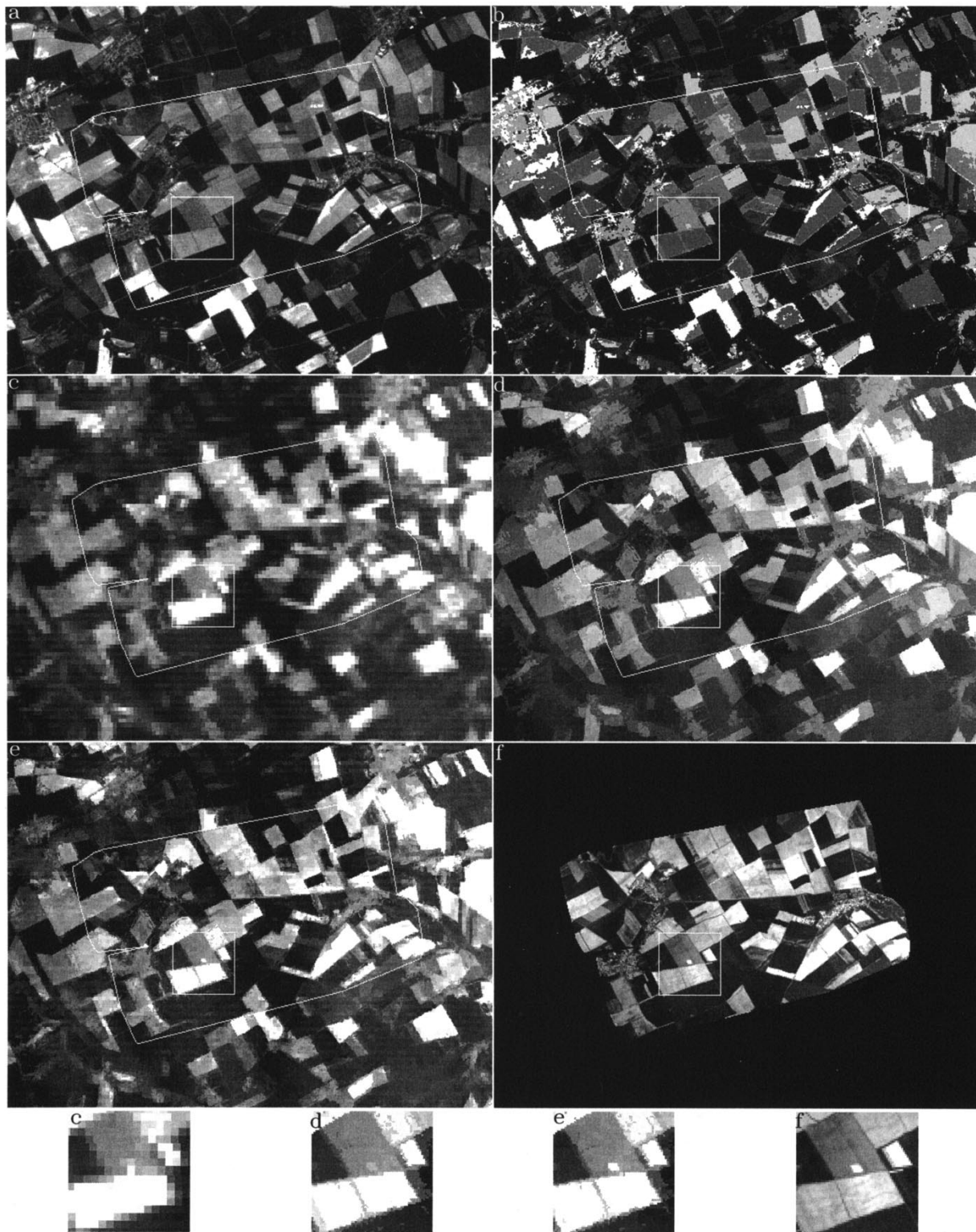


Fig. 5. Unmixing of the real TM image ( $\alpha = 0.5$ ,  $K_0 = 16$ ): (a) high-resolution image in band 3 ( $0.63\text{--}0.69\ \mu\text{m}$ ); (b) classification map with 16 classes; (c) original low-resolution thermal image; (d) thermal image after the unconstrained unmixing; (e) thermal image after the constrained unmixing; (f) reference high-resolution thermal image as simulated from the DAIS-7915 data. Below—zoomed fragments of images (c)–(f) as indicated by the square frame.

The level of the striping noise in the real TM thermal image corresponds to the noise coefficient of  $\sim 0.1$ . This noise together with possible relative coregistration and PSF-calibration errors of within 0.1–0.2 could explain the obtained difference in the unmixing errors between the simulated and real TM images in Figs. 2 and 3.

The unmixing of the real TM thermal image is illustrated in Fig. 5 for the case of  $\alpha = 0.5$  and  $K_0 = 16$ . It shows one of the high-resolution images [Fig. 5(a)] that were used to obtain a high-resolution classification map [Fig. 5(b)]. The classification map was applied to unmix the original TM thermal image [Fig. 5(c)] using the unconstrained [Fig. 5(d)] and constrained

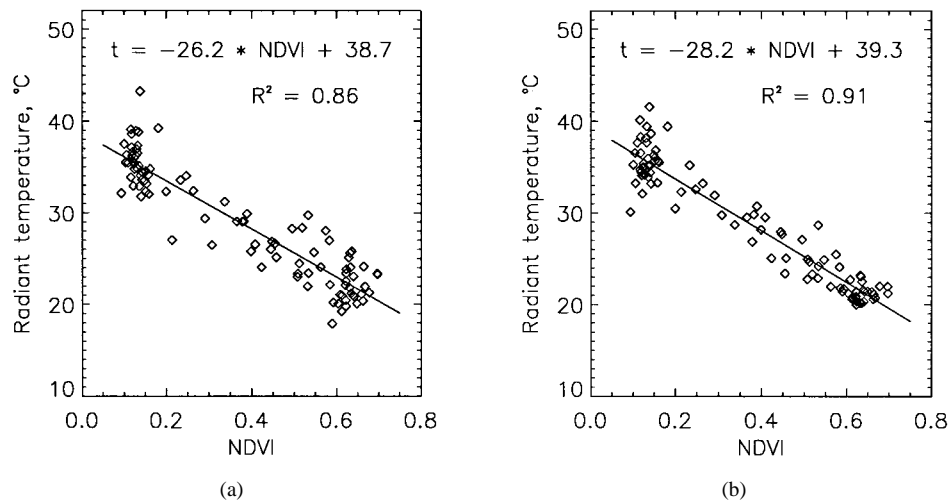


Fig. 6. Relation between the NDVI and the radiant temperature of agricultural fields as obtained from (a) the real merged TM image and from (b) the reference image.

TABLE II  
ACCURACY OF THE MMT-UNMIXING OF THE  
SIMULATED AND REAL TM THERMAL IMAGES

Image	Standard deviation from the reference image, Kelvin			
	Original	Median sharpening	Unconstrained unmixing	Constrained unmixing
Simulated (noise-free)	2.65	2.48	1.84	1.59
Real	2.53	2.30	1.95	2.22

[Fig. 5(e)] algorithms. The results can be compared with the reference image [Fig. 5(f)] that was simulated from the DAIS-7915 data.

Both the constrained and unconstrained algorithms allowed to sharpen the original TM image. The unconstrained unmixing removed also the striping noise of the original image due to its averaging effect within the window. Since it performs the averaging only within the classes, it preserves the sharpness of the class borders. On the contrary, the constrained unmixing preserved all the features of the original image at the scale of the initial thermal pixel size, including the noise. In some cases it allowed to restore more accurately small features. As an example, a zoomed fragment of images Fig. 5(c)–(f) with a small patch of freshly ploughed soil on a green field is shown in the lower part of Fig. 5. The patch is practically not resolved in the original image. Though it is resolved by the unconstrained algorithm, its contrast is much lower than in the reference image. The constrained algorithm allowed to restore the contrast much better.

The unmixing errors in this case are compared in Table II with the accuracy of the original TM thermal image as well as with the accuracy of the median-sharpened image. In order to illustrate the effect of the sensor errors, the unmixing errors of the noise-free simulated image are also indicated. The error of the constrained unmixing in the noise-free case of 1.59 K was lower than of the unconstrained unmixing (1.84 K). The both algorithms provided a significant improvement over

the accuracy of the original image (2.65 K). The median sharpening was not effective for this scene due to a large number of mixed pixels.

During the unmixing of the real noisy TM image, the unconstrained algorithm allowed to obtain a higher overall accuracy of 1.95 K than the other algorithms. It improved significantly the accuracy of the original image (2.53 K). The constrained unmixing was more effected by the noise and provided a much lower accuracy of 2.22 K. However, it performed still better than the median sharpening that resulted in the accuracy of 2.30 K.

The unmixed TM thermal band can be fused with its VNIR and SWIR bands at the pixel size of 30 m for a combined interpretation. As an example, Fig. 6(a) shows the relation between the NDVI vegetation index and the mean temperature of the fields in the real TM image after the unconstrained unmixing. For comparison, Fig. 6(b) shows this relation for the same fields as obtained from the reference image. The standard deviation of the mean field temperature between the unmixed and real image was found to be equal to 2.1 K, coinciding with the residual deviation of the real and simulated TM thermal images. Thus, averaging the unmixed image over the fields reduced the unmixing errors to the level where they it could not be quantified at the given accuracy of the reference image.

The regression lines obtained in the both cases are very close. The scattering of the points around the regression lines of up to a few Kelvin characterizes in fact the additional information in the thermal band that cannot be predicted from the NDVI. It accounts for the effects of crop type, surface color, and moisture [28].

### B. Simulated ASTER Image

The future ASTER sensor of the EOS-AM1 mission will have three VNIR channels with the pixel size of 15 m, six short-wave infrared SWIR channels with the pixel size of 30 m, and five TIR channels with the pixel size of 90 m (Table I). It will have an improved spectral discrimination capability, in particular, for mineralogical investigations.

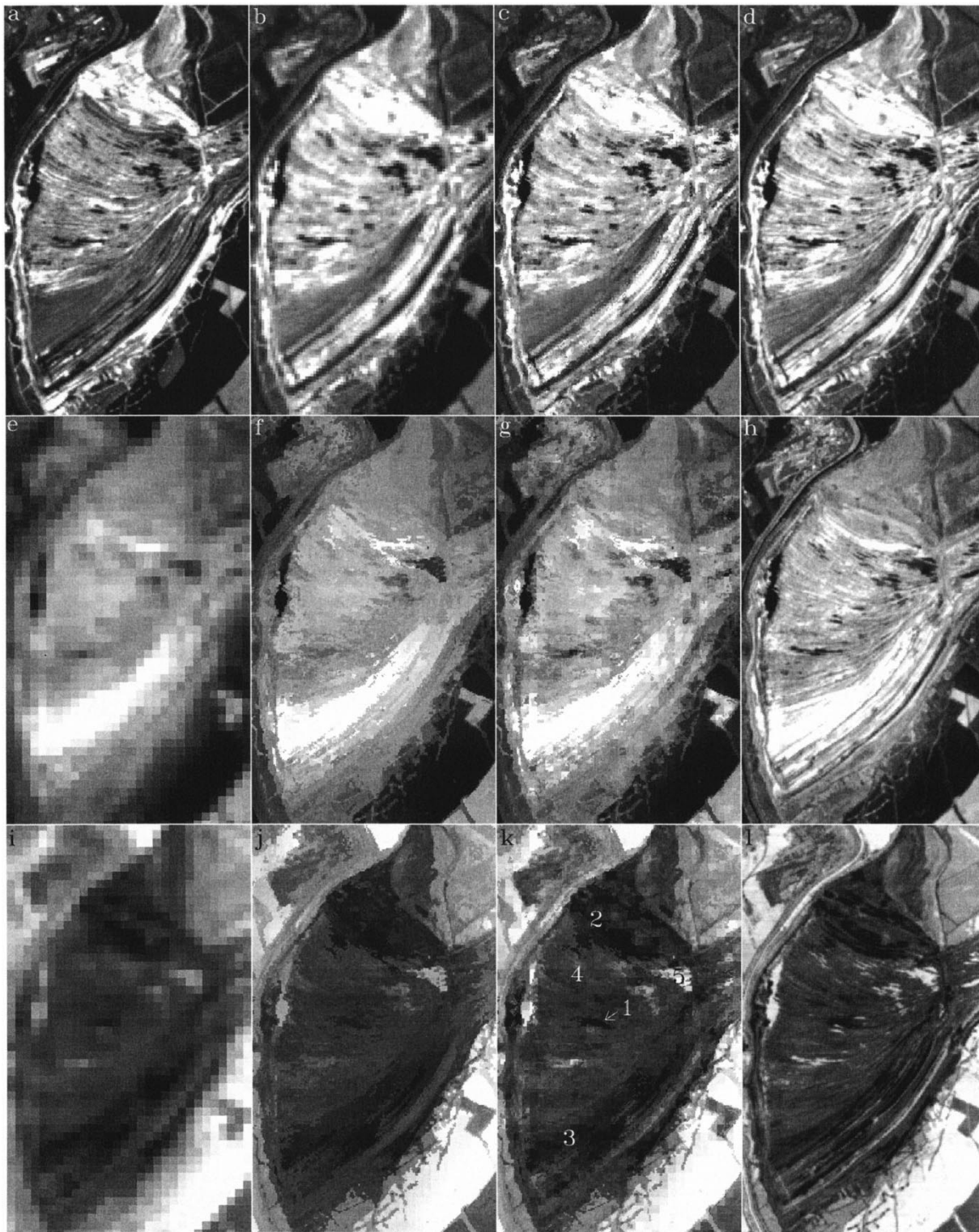


Fig. 7. Unmixing of the simulated ASTER image ( $\alpha = 0.5$ ,  $K_0 = 16$ ): (a) image in VNIR band 2 ( $0.63\text{--}0.69\ \mu\text{m}$ ) with the pixel size of 15 m; (b) original image in SWIR band 6 ( $2.185\text{--}2.225\ \mu\text{m}$ ) with the pixel size of 30 m; (c) image in band 6 after the constrained unmixing; (d) reference image in band 6 with the pixel size of 15 m; (e) original image in TIR band 14 ( $11.0\text{--}12.2\ \mu\text{m}$ ) with the pixel size of 90 m; (f) image in band 14 after the unconstrained unmixing; (g) image in band 14 after the constrained unmixing; (h) reference image in band 14 with the pixel size of 15 m; (i) emissivity image in TIR band 10 ( $8.2\text{--}9.1\ \mu\text{m}$ ) with the pixel size of 90 m; (j) emissivity image in band 10 after the unconstrained unmixing; (k) emissivity image in band 10 after the constrained unmixing; (l) reference emissivity image in band 10 with the pixel size of 15 m.

Unmixing of the ASTER data for mineralogical applications is a critical task for the MMT. The ASTER SWIR bands contain specific absorption features of OH-, H<sub>2</sub>O-, CO<sub>3</sub>-, and SO<sub>4</sub>-bearing minerals that are not encountered in the higher resolution VNIR bands, while its TIR bands cover

specific absorption features of silicates that are not encountered neither in the VNIR nor in the SWIR bands. Thus, in this mineralogical application of the MMT, a classification of the higher resolution bands may be not adequate for unmixing of the lower resolution bands.

We will illustrate the potential and limitations of the MMT in this case on an example of unmixing a simulated ASTER image of the surface lignite mine Zwenkau in Central Germany. Today, the recultivation of such mines becomes a major task, requiring a detailed knowledge of the mineralogical and geochemical composition of the dumped sediments.

The ASTER image was simulated using an airborne hyperspectral image obtained by DAIS-7915 also on May 30, 1996. The ASTER VNIR and SWIR spectral bands could be fitted by the DAIS-7915 bands very accurately. However, no spectral fitting could be performed for the ASTER TIR bands since the corresponding DAIS-7915 bands are too broad for this purpose. That is why the original DAIS-7915 TIR bands 8.2–9.1, 9.1–9.8, 9.8–10.6, 10.4–11.4, and 11.0–12.2  $\mu\text{m}$  were taken to represent approximately the ASTER TIR bands 10–14 despite a significant difference in their location and width. After the spectral band simulation, the geometric resolution of the DAIS-7915 images was degraded to the specified ASTER channel resolution, assuming the Gaussian PSF with the  $2\sigma$ -size equal to the sampling step of the corresponding channel.

The following sensor-related errors were added to the simulated image in accordance to the ASTER sensor specification [44]:

- 1) Gaussian noise with the signal-to-noise ratio (SNR) of 50 (as defined relative the mean band signal) in the VNIR and SWIR and with the noise-equivalent temperature of 0.2 K in the TIR,
- 2) coregistration errors were simulated by introducing interchannel shifts in the direction of both lines and columns of: 0—for channels 1, 4, 7, 12;  $-0.1$  of the sampling step—for channels 2, 5, 8, 10, 13; and  $0.1$  of the sampling step for channels 3, 6, 9, 11, 14.

In order to simulate an error in the ASTER sensor PSF, the unmixing was performed with a 10%-wider PSF than the one assumed for the image simulation.

Reference images with the resolution of 15 m were also simulated for the ASTER SWIR and TIR bands to check the unmixing errors.

Since the ASTER sensor has three resolution levels, the unmixing was conducted in two steps: 1) unmixing of the SWIR image using the higher-resolution VNIR image and 2) unmixing of the TIR image using the merged higher-resolution VNIR/SWIR image. It was found also in this case that the unmixing error is minimal and little sensitive to the total number of classes in the classification map in the range of  $K_0 = 10$ –20. It corresponds to the mean value of  $K = 5$ –8 classes in the  $5 \times 5$  SWIR image windows and of  $K = 8$ –14 classes in the  $5 \times 5$  TIR images windows (the mean number of classes in the central MI pixel was 3–5 and 6–10, respectively). The optimal values of the regularization parameter  $\alpha$  were again 0.3–0.5.

The unmixing results are illustrated in Fig. 7 for the case of  $K_0 = 16$  and  $\alpha = 0.5$ . The unmixing errors are given in Table III.

In the first step, the 3-band VNIR image with the pixel size of 15 m [one of the band images is shown in Fig. 7(a)] was classified and used to unmix the 6-band SWIR image with

TABLE III  
ACCURACY OF THE MMT-UNMIXING OF THE SIMULATED ASTER IMAGE

Parameter	Standard deviation from the reference image			
	Original	Median sharpening	Unconstrained unmixing	Constrained unmixing
Reflectance (mean for SWIR bands 4–8)	0.0179	0.0228	0.0207	0.0168
Radiant temperature (TIR band 14), K	1.47	1.49	1.34	1.23
Emissivity (TIR band 10)	0.0098	0.0091	0.0079	0.0081

the pixel size of 30 m. The unmixing results are illustrated in Fig. 7(b)–(d) for ASTER band 6 (2.185–2.225  $\mu\text{m}$ ) that covers the absorption band of OH-bearing minerals. While the original image [Fig. 7(b)] looks somewhat smeared, its constrained unmixing [Fig. 7(c)] allowed to restore partially its sharpness [compare with the reference image in Fig. 7(d)]. The error of the image unmixed by the constrained algorithm (0.0168 in at-ground reflectance units) was lower than of the original image (0.0179). However, the unconstrained algorithm resulted in a higher error than even the original image (0.0207) since the effect of sharpening at the resolution ratio of two did not compensate for the effects of within-class window averaging and of the retrieval errors. The accuracy of the median sharpening was even lower (0.0228).

The SWIR image as unmixed by the constrained algorithm was merged with the VNIR image at the pixel size of 15 m. This merged 9-band image was classified again and used to unmix the 5-band TIR image with the pixel size of 90 m. Fig. 7(e)–(h) illustrate the unmixing in band 14 (11.0–12.2  $\mu\text{m}$  by our simulation). This spectral band represents surface temperature variations since it is little affected by emissivity variability [45]. Though the original image is very blurred [Fig. 7(e)], many larger temperature variations are restored both by the unconstrained and constrained algorithms [Fig. 7(f), (g)]. Smaller features, in particular the ripple-type patterns within the southern part of the dump were not resolved at the given MI/CI resolution ratio of 6 [compare with the reference image in Fig. 7(h)].

The unconstrained unmixing [Fig. 7(f)] suppressed the sensor noise that can be identified as a blocky structure in some parts of the constrained-unmixed image [Fig. 7(g)]. However, that was possible at the expense of additional spatial averaging, resulting in reducing contrast of small-scale temperature variations in comparison to the constrained unmixing. As a result, the unmixing error of the unconstrained algorithm (1.34 K) was larger than of the constrained one (1.23 K). The error of the median-sharpening (1.49 K) was again larger than of the original image (1.47 K) due to a large number of mixed pixels.

For many mineralogical applications, emissivity variations rather than temperature are of primary interest. We investigated the effect of unmixing on emissivity using band 10 (8.2–9.1  $\mu\text{m}$  by our simulations) that covers the so-called “reststrahlen” bands of quartz. The emissivity in band 10 was retrieved

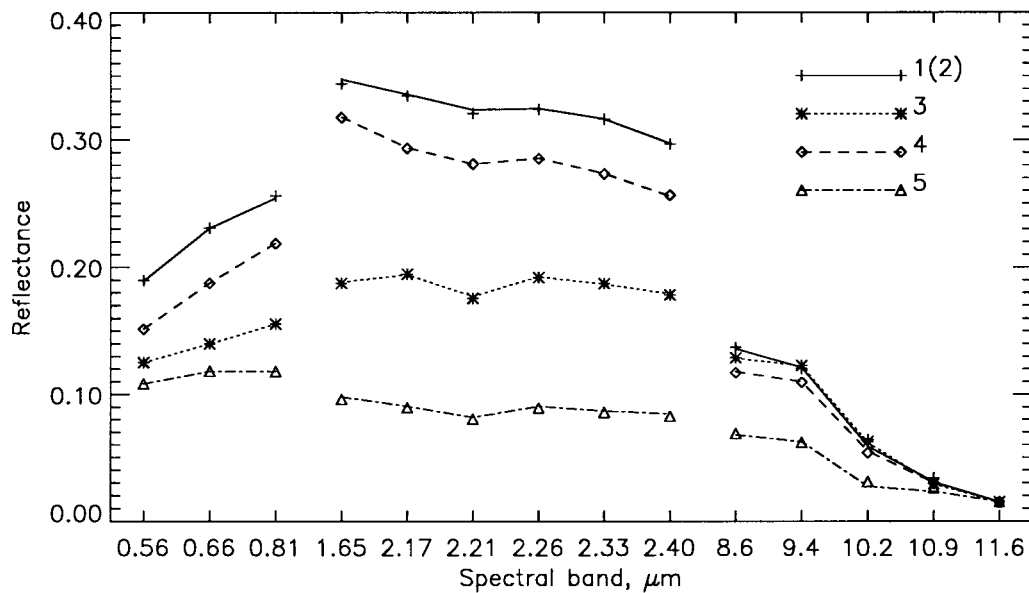


Fig. 8. Reflectance spectra of the areas within the dump that are indicated in Fig. 7(k): lines—spectra from the reference image; signs—spectra from the merged VNIR/SWIR/TIR image.

using the 10/14 band radiance ratio and assuming a constant emissivity of  $\epsilon = 0.985$  in band 14 (the reference channel method as applied to mineralogical investigations [45], [46]).

Fig. 7(i)–(l) show the “emissivity images” in channel 10 as derived from the original [Fig. 7(i)], unmixed [Fig. 7(j), (k)] and reference [Fig. 7(l)] TIR images. We will analyze them only within the mine area since for other objects in the scene (agricultural fields, houses), the assumption about the emissivity value in channel 14 may not be correct. Though the image rationing has increased the noise that can be recognized by a blocky structure in the constrained-unmixed image [Fig. 7(k)], a significant improvement of sharpness and a reasonable correspondence of larger emissivity variations to the reference image can be noticed. The large darker features corresponding to high quartz concentrations are clearly seen in the northern as well as in the southern areas of the dump. A few smaller dark features can be noticed also in the center. The bright spots in the emissivity images match the dark spots in the reflective images and correspond to moist soil. The fine ripple-type pattern, which was not reproduced in the unmixed temperature images, could not be reproduced also in the emissivity images.

The unconstrained unmixing [Fig. 7(j)] resulted in an additional reduction of contrast of small features in comparison to the constrained algorithm [Fig. 7(k)]. However, since it is less sensitive to the increased noise, its overall accuracy was even a little better than of the constrained unmixing (0.0079 versus 0.0081). The error of median sharpening (0.0091) was higher than of the MMT-unmixing but lower than of the original image (0.0098).

The constrained-unmixed SWIR and TIR images were merged with the VNIR image at the pixel size of 15 m and used to analyze the spectra of some features within the mine in the whole spectral range covered by the ASTER sensor. The

location of these features is indicated in Fig. 7(k) and their spectra in the unmixed and reference images are compared in Fig. 8. The reflectance values in the TIR were obtained as one minus emissivity (Kirchhoff’s law).

Averaging over the feature area has again drastically smoothed out the pixel-level unmixing errors. Even the small dark feature 1 in the center of the emissivity image does not show any significant deviation between the unmixed and reference spectra. Its spectrum coincides with the spectrum of the large area 2 in the northern part of the dump (it is not shown separately). The both areas show the maximal quartz concentration. Area 3 in the southern part of the dump has a significantly lower reflectance in the VNIR and SWIR and shows a little lower quartz concentration than areas 1 and 2. The absorption feature at  $2.2 \mu\text{m}$ , which is typical for clay minerals, is best pronounced in this area. The central part of the dump (area 4) shows the smallest quartz concentration. However, its VNIR and SWIR reflectance spectra lie between those of areas 1(2) and 3. It illustrates by the way the case when linear statistical predictors could lead to an inversion of the quartz concentration contrast.

The spectrum of the moist area 5 is dominated by water and was not used for a mineralogical interpretation.

The restoration of some emissivity variations related to quartz concentration may be explained by a local statistical predictability. Quartz does not have absorption features in the VNIR and SWIR bands that were used for the classification. However, the mixture of stratigraphically and petrographically different sediments may have caused simultaneous local variations in the quartz concentration and in the content of the minerals recognizable in the VNIR/SWIR and/or in the surface structure. As a result, the features, that are recognizable in the higher-resolution VNIR/SWIR images, proved to have different spectra also in the TIR. The interpretation of their TIR

spectra in terms of quartz concentration helped to characterize these VNIR/SWIR features.

## VI. CONCLUSIONS

- 1) The application of the MMT unmixing to a real TM image as well as to a simulated ASTER image has demonstrated a significant improvement in sharpness and radiometric accuracy in comparison to the original images. The MMT unmixing accuracy was also significantly better than the accuracy of the median-sharpening predictor in the conditions when the images were dominated by mixed pixels.
- 2) The constrained MMT unmixing preserves all the available radiometric information of the low-resolution MI image and performs better at a low noise level and for smaller objects. On the other hand, the unconstrained MMT unmixing performs better at a high noise level and can be used to suppress noise in the original image. The advantage of the unconstrained MMT algorithm in comparison to other noise filtering techniques is that it performs averaging only within the class areas in the window and thus preserves the sharpness of the classification map.
- 3) The MMT unmixing can be performed only relative those classes that can be recognized in the high-resolution CI image. If a class is homogeneous only in the CI spectral bands but heterogeneous in the MI bands, averaging of its MI signature will take place over the class area in the window (with accounting for all available low-resolution MI information by the constrained algorithm). If class areas with different MI signatures are located in different windows, they will be treated independently and no averaging of their MI signatures will take place. Thus, the MMT unmixing can be efficient for a specific application if the classes, which are essential for this application, can be differentiated spectrally in CI data and/or can be separated spatially.
- 4) When analyzing usefulness of the MMT unmixing for a specific application, a possible local correlation has to be taken into account between phenomena that are recognizable in the CI and MI spectral bands. The importance of the local correlation has been demonstrated on the example of unmixing some quartz-related emissivity variation using the VNIR/SWIR bands for classification.
- 5) The borders of features in the unmixed images are defined principally by the high-resolution classification map but may be modified by signal variations in the lower-resolution MI bands. MI/CI data fusion for these features may enable their improved characterization in comparison to the information available in the CI bands. It was illustrated on examples of merging: 1) NDVI and temperature measurements for agricultural fields and 2) VNIR/SWIR spectral variations and emissivity variations related to quartz concentration in a lignite mine surface material.
- 6) The MMT unmixing of the TM and ASTER images demonstrated its capability to provide the radiometric

accuracy at the high-resolution pixel level of between 1.2 and 2.0 K, depending on a scene and on sensor-related errors. The unmixing accuracy for emissivity in the quartz-absorption band was  $\sim 0.008$ , making it possible to differentiate a few gradations of quartz concentration. A further improvement in the retrieval accuracy can be achieved if the unmixed images are interpreted at the level of features that can be recognized in them.

- 7) The analysis of the MMT sensitivity to sensor errors showed that the strongest requirement is the accuracy of geometric coregistration of the data; the coregistration errors should not exceed 0.1–0.2 of the linear pixel size of the low-resolution image. This is a strong but not unrealistic requirement to modern coregistration techniques [47].
- 8) The performed simulation of the ASTER data fusion shows the application potential of the MMT unmixing for fusion of multispectral and multiresolution VNIR/SWIR/TIR data to be expected from new satellite sensors in the near future.

## ACKNOWLEDGMENT

The authors would like to thank Dr. M. von Schönemark (DLR-Institute of Space Sensor Technology) for providing the TM image and the on-ground temperature measurements. They are grateful to the anonymous reviewers for their comments that helped improve the final version of the paper.

## REFERENCES

- [1] "Fusion of earth data: Merging point measurements, raster maps, and remotely sensed images," T. Ranchin and L. Wald, Eds., in *Proc. Int. Conf.*, Cannes, France, Feb. 6–8, 1996.
- [2] "Fusion of earth data: Merging point measurements, raster maps, and remotely sensed images," T. Ranchin and L. Wald, Eds., in *Proc. Second Int. Conf.*, Sophia Antipolis, France, Jan. 28–30, 1998.
- [3] C. Pohl and J. L. Van Genderen, "Multisensor image fusion in remote sensing: Concepts, methods and applications," *Int. J. Remote Sensing*, vol. 19, no. 5, pp. 823–854, Mar. 1998.
- [4] J. Vrabel, "Multispectral imagery band sharpening study," *Photogramm. Eng. Remote Sensing*, vol. 62, no. 9, pp. 1075–1083, Sept. 1996.
- [5] T. J. Patterson and M. E. Bullock, "Radiometrically correct sharpening of multispectral images using a panchromatic image," *Proc. SPIE*, vol. 2234, pp. 252–264, 1994.
- [6] N. D. A. Mascarenhas, G. J. F. Banon, and A. L. B. Candeias, "Multispectral image data fusion under a Bayesian approach," *Int. J. Remote Sensing*, vol. 17, no. 8, pp. 1457–1471, May 1996.
- [7] H. N. Gross and J. R. Schott, "Application of spectral mixture analysis and image fusion techniques for image sharpening," *Remote Sens. Environ.*, vol. 63, no. 2, pp. 85–94, Feb. 1998.
- [8] V. K. Shettigara, "A generalized component substitution technique for spatial enhancement of multispectral images using a higher resolution data set," *Photogramm. Eng. Remote Sensing*, vol. 58, no. 5, pp. 561–567, May 1992.
- [9] H. J. M. Pellemans, R. W. L. Jordans, and R. Allewijn, "Merging multispectral and panchromatic SPOT images with respect to the radiometric properties of the sensor," *Photogramm. Eng. Remote Sensing*, vol. 59, no. 1, pp. 81–87, Jan. 1993.
- [10] R. Haydn, G. W. Dalke, J. Henkel, and J. E. Bare, "Application of the IHS color transformation to the processing of multisensor data and image enhancement," in *Proc. Int. Symp. Remote Sensing of Arid and Semi-Arid Lands*, Cairo, Egypt, 1982, pp. 599–616.
- [11] H. Kaufmann, "Mineral exploration along the Aqaba-Levant structure by use of TM-data: Concepts, processing and results," *Int. J. Remote Sensing*, vol. 9, no. 10–11, pp. 1639–1658, 1988.
- [12] P. S. Chavez, S. C. Sides, and J. A. Anderson, "Comparison of three different methods to merge multiresolution and multispectral data:



- Landsat TM and SPOT panchromatic," *Photogramm. Eng. Remote Sensing*, vol. 57, no. 3, pp. 295–303, Mar. 1991.
- [13] C. Conese, F. Maselli, and T. De Filippis, "A new method for the integration of Landsat TM and SPOT panchromatic data," *Int. Arch. Photogramm. Remote Sensing*, ISPRS Commission 3, vol. 29, pt. B3, pp. 892–895, 1992.
  - [14] R. A. Schowengerdt, "Reconstruction of multispatial, multispectral image data using spatial frequency content," *Photogramm. Eng. Remote Sensing*, vol. 46, no. 10, pp. 1325–1334, Oct. 1980.
  - [15] V. T. Tom, M. J. Carlotto, and D. K. Scholten, "Spatial sharpening of thematic mapper data using a multiband approach," *Opt. Eng.*, vol. 24, no. 6, pp. 1026–1029, Nov./Dec. 1985.
  - [16] T. Ranchin, L. Wald, and M. Mangolini, "Efficient data fusion using wavelet transform: The case of SPOT satellite images," *Proc. SPIE*, vol. 2034, pp. 171–178, 1993.
  - [17] H. Li, B. S. Manjunath, and S. K. Mitra, "Multisensor image fusion using the wavelet transform," *Opt. Models Image Process.*, vol. 57, no. 3, pp. 235–245, May 1995.
  - [18] D. A. Yocky, "Image merging and data fusion by means of the discrete two-dimensional wavelet transform," *J. Opt. Soc. Amer.*, vol. 12, no. 9, pp. 1834–1841, Sept. 1995.
  - [19] B. Garguet-Dupont, J. Girel, J.-M. Chassery, and G. Pautou, "The use of multiresolution analysis and wavelets transform for merging SPOT panchromatic and multispectral image data," *Photogramm. Eng. Remote Sensing*, vol. 62, no. 9, pp. 1057–1066, Sept. 1996.
  - [20] A. E. Iverson and J. R. Lersch, "Adaptive image sharpening using multiresolution representations," *Proc. SPIE*, vol. 2231, pp. 72–83, 1994.
  - [21] L. Alparone, V. Cappellini, L. Mortelli, B. Aiazzi, S. Baronti, and R. Carla, "A pyramid-based approach to multisensor image data fusion with preservation of spectral signatures," in *Future Trends in Remote Sensing (Proc. 17th EARSeL Symposium)*, Lyngby, Denmark, June 17–19, 1997, P. Gudmandsen, Ed. Rotterdam, The Netherlands: Balkema, 1998, pp. 419–426.
  - [22] L. Borriello, "SPOT imagery: A Fourier-based approach to panchromatic and multispectral data integration," *Proc. Int. Symp. Machine Processing of Remotely Sensed Data*, 1984.
  - [23] D. Pradines, "Improving SPOT images size and multispectral resolution," *Proc. SPIE*, vol. 660, pp. 98–102, 1986.
  - [24] C. K. Munechika, J. S. Warnick, C. Salvaggio, and J. R. Schott, "Resolution enhancement of multispectral image data to improve classification accuracy," *Photogramm. Eng. Remote Sensing*, vol. 59, no. 1, pp. 67–72, Jan. 1993.
  - [25] J. P. Price, "Combining panchromatic and multispectral imagery from dual resolution satellite instruments," *Remote Sens. Environ.*, vol. 21, no. 2, pp. 119–128, Mar. 1987.
  - [26] R. Nishii, S. Kusanobu, and S. Tanaka, "Enhancement of low spatial resolution image based on high resolution bands," *IEEE Trans. Geosci. Remote Sensing*, vol. 34, pp. 1151–1158, Sept. 1996.
  - [27] B. Z. Petrenko, "Robust restoration of microwave brightness contrasts from the DMSP SSM/I data," in *Proc. IGARSS'96*, July 1996, pp. 481–483.
  - [28] S. M. Moran, "A window-based technique for combining Landsat Thematic Mapper thermal data with higher-resolution multispectral data over agricultural lands," *Photogramm. Eng. Remote Sensing*, vol. 56, no. 3, pp. 337–342, Mar. 1990.
  - [29] K. Steinnocher, "Application of adaptive filters for multisensoral image fusion," in *Proc. IGARSS'97*, Aug. 1997, pp. 910–912.
  - [30] J. B. Adams, M. O. Smith, and P. E. Johnson, "Spectral mixture modeling: A new analysis of rock and soil types at the Viking Lander I site," *J. Geophys. Res.*, vol. 91, no. B8, pp. 8098–8112, July 1986.
  - [31] A. R. Gillespie, M. O. Smith, J. B. Adams, and S. C. Willis, "Spectral mixture analysis of multispectral thermal infrared images," *Proc. Second Thermal Infrared Multispectral Scanner (TIMS) Workshop*, June 6, 1990, pp. 57–74.
  - [32] J. J. Settle and N. A. Drake, "Linear mixing and the estimation of ground cover proportions," *Int. J. Remote Sensing*, vol. 14, no. 6, pp. 1159–1177, Apr. 1993.
  - [33] B. Zhukov and D. Oertel, "A technique for combined processing of the data of an imaging spectrometer and of a multispectral camera," *Proc. SPIE*, vol. 2480, pp. 453–465, Apr. 1995.
  - [34] ———, "Multi-sensor multi-resolution technique and its simulation," *Zeitschrift Photogramm. Fernerkundung*, no. 1, pp. 11–21, Jan. 1996.
  - [35] Ph. Puyou-Lascassies, A. Podaire, and M. Gay, "Extracting crop radiometric responses from simulated low and high spatial resolution satellite data using a linear mixing model," *Int. J. Remote Sens.*, vol. 15, no. 18, pp. 3767–3784, Dec. 1994.
  - [36] B. Zhukov, M. Berger, F. Lanzl, and H. Kaufmann, "A new technique for merging multispectral and panchromatic images revealing sub-pixel spectral variation," *Proc. MOMS-02 Symp.*, Köln (Cologne), Germany, Paris, EARSeL, July 5–7, 1995, pp. 163–168.
  - [37] B. Zhukov, D. Oertel, P. Strobl, F. Lehmann, and M. Lehner, "Fusion of airborne hyperspectral and multispectral images," *Proc. SPIE*, vol. 2758, pp. 148–159, Apr. 1996.
  - [38] J. A. Richards, *Remote Sensing Digital Image Analyzes. An Introduction*. Berlin, Germany: Springer-Verlag, 1986.
  - [39] A. Björck, "Least squares methods," *Handbook Numer. Anal.*, vol. 1, pp. 465–647, 1990.
  - [40] *Image Recovery: Theory and Application*, H. Stark, Ed. New York: Academic, 1987.
  - [41] P. C. Hansen, "Numerical tools for analysis and solution of Fredholm integral equations of the first kind," *Inv. Probl.*, vol. 8, pp. 849–872, 1992.
  - [42] B. Zhukov, D. Oertel, and M. Lehner, "TM/LANDSAT thermal image unmixing," *Proc. SPIE*, vol. 3071, pp. 85–96, 1997.
  - [43] S. Chang, M. Westfield, F. Lehmann, D. Oertel, and R. Richter, "79-channel airborne imaging spectrometer," *Proc. SPIE*, vol. 1937, pp. 164–172, 1993.
  - [44] H. Fujisada, "Overview of ASTER instrument on EOS-AM1 platform," *Proc. SPIE*, vol. 2268, pp. 14–36, 1994.
  - [45] A. R. Kahle, "Separation of temperature and emittance in remotely sensed radiance measurements," *Remote Sens. Environ.*, vol. 42, pp. 107–111, 1992.
  - [46] G. Reinhäkel and G. Krüger, "Combined use of laboratory and airborne spectrometry from the reflective to thermal wavelength range for a quantitative analysis of lignite overburden dumps," *Proc. 27th Int. Symp. Remote Sens. Environ.*, Tromsø, Norway, June 8–12, 1998, pp. 507–512.
  - [47] P. Blanc, L. Wald, and T. Ranchin, "Importance and effect of co-registration quality in an example of "pixel to pixel" fusion process," *Proc. Second Int. Conf. Fusion Earth Data*, Sophia Antipolis, France, Jan. 28–30, 1998, pp. 67–73.



Boris Zhukov received the M.Sc. degree in physics in 1975 from the Moscow Physical and Technical Institute, Moscow, USSR, and the Ph.D. degree in geophysics in 1982 from the Main Geophysical Observatory of the USSR.

Since 1975, he has been with the Space Research Institute, Russian Academy of Sciences, Moscow, currently as a Senior Research Scientist. He was a member of the imaging team of the VEGA mission to Halley's Comet and headed the scientific team of the imaging and spectrometric experiment VSK of the PHOBOS mission. From 1992 to 1998, he paid a few extended visits as a Guest Scientist to the DLR Institute of Optoelectronics, Oberpfaffenhofen, Germany. His research interests are in physical principals, mathematical simulation, and data processing of optical remote sensing of the Earth and the planets.



Dieter Oertel received the M.Sc. degree in radio-electronic engineering in 1969 from the Leningrad Electrotechnical Institute, Leningrad, USSR, and the Ph.D. degree in electronics in 1976 and the D.Sc. degree in infrared remote sensing in 1983 from the Academy of Sciences of the German Democratic Republic.

He was the Head of the Optoelectronic Systems branch of the Space Research Institute (IKF), Berlin from 1978 to 1991, leading the development, test and calibration of various aerospace optoelectronic sensors, such as IR-Fourier-Spectrometers and a Wide-Angle Optoelectronic Stereo Scanner (WAOSS), developed primarily for the Mars'96 Mission. Since 1992, he is responsible at the DLR Institute of Optoelectronics, Oberpfaffenhofen, Germany, for the laboratory calibration, improvement, and utilization of the Digital Airborne Imaging Spectrometer DAIS-7915, used in Europe as a Large Scale Facility from 1996 to 1998.



**Franz Lanzl** received the M.Sc. degree in physics in 1959 from the Technical University of Munich, Germany, the Ph.D. degree in nuclear physics in 1964 from the University of Göttingen, Germany, and the D.Sc. degree in holography in 1971 from the Technical University of Darmstadt, Germany.

From 1971 to 1979, he was a Professor of physics, Institute of Applied Physics, University of Hamburg, Germany. Since 1979, he has been the Director of the DLR Institute of Optoelectronics, Oberpfaffenhofen, Germany.

Prof. Lanzl was/is a temporary Vice-President of ICO (International Commission for Optics), Chair of the ICO Committee for the Regional Development of Optics, member of the ESA Meteosat Inquiry Board, member of the Council for the Optical Research Institute, Tübingen, Germany, Head of the German Optical Committee, member of the Expert Committee "High-precision Navigation" of the German Research Society (DFG), and the Principal Investigator of the Modular Optoelectronic Multispectral Stereo Scanner (MOMS) on the PRIRODA Module of the Russian Space Station MIR. He is also responsible for the airborne imaging spectrometer DAIS-7915, which is operational as a Large Scale Facility of the European Union.



**Götz Reinhäckel** received the M.Sc. degree in geology in 1996 from the University of Munich, Germany. Since 1997, he has been a Ph.D. student at the DLR Institute of Optoelectronics, Oberpfaffenhofen, Germany.

His research work is focused on imaging spectrometry. He is mainly involved in quantitative applications using remote sensing and laboratory spectroscopy in the thermal infrared wavelength range.